ICI Design for Geostationary Satellite Imaging

David C. Hyland

Professor Emeritus, Texas A&M University, College Station, Texas

Abstract: Recent advances in the reduction of the integration time required of Intensity Correlation Imaging (ICI) have opened the possibility of significant improvements in astronomical imaging. This paper discusses the application of ICI to the fine resolution imaging of geostationary satellites conducted by ground-based observatories.

1.Introduction

Reviewers who have read the latest papers on the new Intensity Correlation Imaging process have made the excellent suggestion that the author demonstrate how effective this algorithm can be utilized in real applications. Now that the mathematics of the ICI algorithm and its enormous reduction of integration time is reasonably well explored, this paper reviews its practical applications in astronomy, specifically the high resolution imaging of commercial geostationary satellites. This could open the door to the construction of advanced ICI observatories that are within the financial resources of colleges and universities around our country, yet able to compete with very large telescopes such as the 30-meter telescope.

To arrive at a preliminary design for a ICI observatory, Section 2 briefly reviews the sequence of five papers that have completed the present ICI algorithm and its formulation of the integration time. Next, Sections 3 and 4 discuss two additional factors that have been known to reduce integration times still further. These are the use of redundant baselines and multispectral avalanche photodetectors. Finally, Section 5 determines the rapid integration times for high resolution imaging of geostationary satellites. Surprisingly, and due to the partial coherence effect, the architecture of the ICI observatory strongly resembles an imager design found in nature.

2. The evolution of ICI toward its present state

The first experiments on imaging techniques based upon the correlation of intensity fluctuations measured at two or more spatial-temporal points for thermal sources of light were carried out by Hanbury Brown and Twiss (HBT) [1-4]. At the outset a number of advantages were discerned: non diffraction limited, inexpensive hardware, immunity to phase and intensity scintillations, and electronically coupled apertures capable of unlimited resolution. However the very long integration times posed the main obstacle for some seventy years.

Besides the thermal source of illumination, HBT rests on the following assumptions concerning the measurements of the cross correlations of intensity fluctuations :

(1) The square of the normalized coherence magnitude values are typically of order 10^{-3} for those regions in the u-v plane corresponding to reasonably detailed features in the image domain. Hence, the SNR has only a linear term in this factor.

(2) The bandwidth of the photodetector is much less than the optical bandwidth. As a consequence only spectral radiance contributes to the SNR. Furthermore, the one-time probability density of the intensity fluctuations is Gaussian.

(3) The condition of greatest interest to us is the observation of dim objects ranging from 10 to 14 apparent magnitudes. The result is that the SNR has only a linear term in the number density per mode.

(4) Dark count should be negligeable. This means that photodetectors need temperature control. (The author favors built-in coolers).

(5) Photodetectors must have no DC component. The object is to measure intensity *fluctuations*. (The author favors APDs run in Geiger mode)

(6) If individual apertures are larger than the size able to resolve the target, the coherence magnitude washes out. The *partial coherence effect*, denoted P(A), is explained in Section 5 and must be close to unity.

Under these conditions, and following Brown and Twiss [1-4], the intensity fluctuation cross-correlation for a pair of apertures is:

Intensity fluctuation cross correlation for u-v vector $\mathbf{u}$

$$= \kappa^2\eta^2 \frac{\Delta\nu_c}{\Delta\nu_d}\bar{\beta}^2 |\gamma|^2 P(A) + \left[\kappa^2\eta \frac{\Delta\nu_c}{\Delta\nu_d}\bar{\beta}\right]\frac{1}{\sqrt{\Delta T \Delta\nu_d}} N_{\mathbf{u}}(0,1)$$

where:

$\bar{\beta}$ = Number density per mode $\cong AI/\Delta\nu_c$

A = Aperture area

I = Number of photon arrivals per square meter, per second

$|\gamma|$ = Normalized coherence magnitude $\cong 10^{-3}$

$\Delta\nu_c$ = Optical bandwidth

$\Delta\nu_d$ = Detector bandwidth

κ = Magnitude of detector response over $1/\Delta\nu_d$

η = Photon detection efficiency

$N_{\mathbf{u}}(0,1)$ = Gaussian random variable with zero mean and unit standard deviation. $N_{\mathbf{u}}(0,1)$ and $N_{\mathbf{u}'}(0,1)$ are statistically independent if $\mathbf{u} \neq \mathbf{u}'$. (1. a-l)

$P(A)$ = Partial coherence effect

ΔT = Integration time. The same for all aperture pairs.

At this point we observe that the coefficient of the noise term can be determined at the outset by calibrating the detectors, using the aperture parameters, and measuring the intensity observed by the individual aperture sensors. In other words, the quantity $\left[\kappa^2\eta\bar{\beta}\Delta\nu_c/\Delta\nu_d\right]/\sqrt{\Delta T\Delta\nu_d}$ can be obtained before any intensity fluctuation cross correlation measurements are attempted. Hence, it is convenient to divide the intensity cross-correlation by this factor, thereby normalizing the noise component to unity standard deviation. Therefore we can write:

$$S(\mathbf{u}) = \frac{\text{Intensity fluctuation cross correlation}}{\left[\kappa^2\eta\bar{\beta}\Delta\nu_c/\Delta\nu_d\right]/\sqrt{\Delta T\Delta\nu_d}} = S_0\sqrt{\Delta T}\,|\gamma(\mathbf{u})|^2 + N_{\mathbf{u}}(0,1) \qquad \text{(2.a,b}$$

$$S_0 = \eta\bar{\beta}\sqrt{\Delta\nu_d}\,P(A)$$

S_0 may be recognized as the zero baseline SNR for a unit integration time, which can be determined at the outset via measurements from the individual apertures and equipment calibrations. $S(\mathbf{u})$ can be interpreted as the "empirical SNR" that one can use to compare the signal component of the measurement to the noise component, whose standard deviation is always one. Hence, as the integration time increases, one can compare $S_0\sqrt{\Delta T}\left|\gamma(\mathbf{u})\right|^2$ to unity to ascertain if the desired SNR is reached with 50% probability. Thus we can define ΔT as:

$$SNR_d \equiv E\left[S(\mathbf{u})\right] = S_0\sqrt{\Delta T}\left|\gamma(\mathbf{u})\right|^2 \;\Rightarrow\; \Delta T = \left[\frac{SNR_d}{S_0\left|\gamma(\mathbf{u})\right|^2}\right]^2 \tag{3}$$

The expression for ΔT constitutes the "conventional" estimate of the integration time formulated by Brown and Twiss.

The effort to reduce integration times lasted over a quarter of a century and success was achieved quite recently via a sequence of five journal papers [6-10]. The history of this labor has been disclosed by the invited speech, [11], at the 4th International Conference on Optics, Photonics and Lasers at Hiroshima, Japan on December 7, 2023. The following briefly describes the evolution of an algorithm that enormously reduces integration time, rendering ICI a practical, and inexpensive astronomical imaging technique.

The first challenge was to discover a phase retrieval algorithm capable of converging in the presence of large amounts of noise (low values of SNR_d). The starting point of this effort was Fienup's Hybrid Input-Output (HIO) algorithm [5]. In the presence of low noise HIO displays superior convergence behavior in contrast to other methods. If SNR_d is below unity, however, HIO can often fail to converge. In references [6,7] the present author added two crucial lines of code to HIO: (1) a strict restriction of real valued, non-negativity on the current image every iteration and (2) a relaxation technique that gradually satisfies both Fourier and image domain constraints. If we denote by $\hat{G}(k)$ the current value of the coherence magnitude, then the relaxation technique is:

$$\hat{G}(k+1) = (1-\varepsilon)\hat{G}(k) + \varepsilon\left|\Im \mathrm{g}(k)\right| \tag{4}$$

Where $\left|\Im \mathrm{g}(k)\right|$ is the magnitude of the Fourier transform of the earlier image iterate, $\mathrm{g}(k)$ and the relaxation parameter, ε is of order 10^{-5} to 10^{-6}. The resulting algorithm is called the Noise Reduction Phase Retrieval (NRPR) algorithm.

The analysis of Reference [7] shows that the alteration of the original coherence magnitude data using the previous iterate reduces the noise. Examples shown in [6] display full convergence to the noise-free image for SNR_d as low as 10^{-8}. Moreover, [7] establishes that full convergence is attained provided that zero amplitude pixels are known *a priori.*

As a next step, we note that Brown and Twiss wished to determine stellar diameters on the basis of an assumption of radial symmetry which requires only the coherence magnitudes for each flux collector pair. However, for two-dimensional imaging the Van Cittert-Zernike theorem requires phase information, which in turn demands low noise phase retrieval algorithms as provided by [6,7]. Assuming that black pixels are known *a priori*, the Fisher information needed for the Cramer-Rao bound demands the use of conditional probabilities reflecting the necessary constraints. Such probabilistic constraints necessarily reduce noise.in the final result. This is demonstrated in Reference [8]. Using the Hirschman entropic uncertainty principle [12-14] and Lyapunov's form of the central limit theorem [15], the following asymptotic relation (for large numbers of black pixels) is obtained:

$$N_C SNR \cong 4\sqrt{2} \tag{5}$$

Where we set SNR_d to unity and N_C is the number of black pixels in the field of view. We note that even for modest sized images, N_C is quite large and dominates the total pixel count. Therefore, the asymptotic result for the integration time established for NRPR is:

$$\left(\Delta T\right)_{NRPR} \cong \left(\frac{4}{N_C S_0 \left|\gamma\right|_{\min}^2}\right)^2 \tag{6}$$

Figure 1 shows the ratio of $\left(\Delta T\right)_{NRPR}$ to the conventional calculation of Brown and Twiss, $\left(\Delta T\right)_{Conventional}$.

Fig. 1. The ratio of NRPR integration time estimates to the conventional estimate of Brown and Twiss.

The previous expressions presuppose that the configuration of the zero intensity pixels are known. But our final goal is to use ICI to construct images with reasonable integration times using no *a priori* data except that (1) we are looking at bright objects against a black sky, and (2) we have a crude estimate of the angular size of the objects (±3 dB). Thus we must find a way to discover the identity of the black pixels from the limited data (items 1 and 2).

Reference [9] explores a stochastic search algorithm. Using the same initial coherence magnitude data, run a series of NRPR calculations, where the initial guesses for the image are statistically independent, uniformly distributed in an interval [0,δ), where δ is a real, nonnegative constant. This produces an ensemble encompassing all possible multi-pixel images. One might reason that such an hypothesis test would demand innumerable trials. Surprisingly, there is a high probability that the number of trials needed to discover the black pixels (and converge to the noise-free image) are very few.

The key element in the stochastic search algorithm is the concept of the "Box". This is a square region of size Bx that is centered in the field of view where all pixels within the box are unconstrained and all pixels outside the box are constrained to be zero. The basic idea is to set up a series of NRPR runs that start with large box sizes and progress to smaller and smaller boxes – until the noise-free image is identified.

Figure 2 shows the process. One first collects the coherence magnitude data for all apertures. This data remains the same for all random trials. The algorithm sets a box size, then runs NRPR (using a new random initial guess every trial). If, during a sequence of trials there are no two fully correlated images, the algorithm tries a new, smaller box and runs again. On the other hand, if during a sequence of trials there are two identical images (allowing for the trivial ambiguities of 180 degree rotation or object translation in the field of view), then NRPR has selected the noise-free image. Every computation made to date using this algorithm has produced the same result. As in thousands of similar tests, there are two categories of images: A set of random, nonrepeatable images and a set of images that, aside from translations and 180-degree rotations, perfectly match one another (and match the true, noise-free image as is proved in Ref. 10).

To illustrate computational results for the stochastic search algorithm, Figure 3 shows a typical sequence of random trials (for a simple satellite image) terminating in the perfect noise-free image. Figure 4 displays the statistics of the probability that for a given box size the algorithm will identify the correct image after R trials. The probabilities are quite large. The Right side of the Figure shows that if the box size is too small to capture the true image, the resulting converged image produces illumination outside the box as a consequence of a conflict between the Fourier domain and image domain constraints.

Figure 2: Diagram of the stochastic search algorithm.

Figure 3: Typical sequence of convergent images (for the box size of 44), terminating when two of the images are perfectly correlated.

Figure 4: Left-hand side: Monte Carlo statistics of the probability of a noise-free image identification vis the stochastic search algorithm. Right-hand side: The algorithm indicates when the box-size is too small to contain the illuminated object.

Finally, Reference 10 presented a sequence of asymptotic approximations revealing the underlying mechanisms of ICI and its attendant NRPR algorithm and the stochastic search algorithm as published in [9]. The intent is to better understand the ICI approach with a view to improve and refine the algorithms. The outcome is that [10] provides proof of the results of [9]. The developments in section 6 of [10] reveal why the stochastic search process can achieve convergence to the noise-free image with high probability and few computational trials. As a result of the statistical analysis of Section 6 of [10], it turns out that the reverse of the stochastic algorithm, i.e. starting with small boxes and then increasing their size as opposed to vice-versa actually speeds up the convergence of the method to a handful of trials. These results are illustrated in Figure 5.

Figure 5: (a) GOES 16 type geophysical satellite at geostationary orbit with 20 cm resolution, (b) Closed-form statistics of the stochastic search algorithm, (c) A sequence of images of the test image proceeding from left to right and top to down. The top row progresses from $B_x = 20$ to $B_x = 28$ illustrating the contradictions inherent when the box size is smaller than the illuminated object. Once the box size can contain the object the lower row shows five correct images, all using $B_x = 30$

3. Preliminary observatory design and the use of redundant baselines

Having reviewed the up-to-date ICI theory, this paper addresses the characteristics of an observatory suited to the high resolution imaging of commercial geostationary satellites. For simplicity, it is assumed that the tilt of the u-v plane from zenith is modest, so that the positioning of the observatory apertures is approximately on the horizontal ground plane. The geometry of the observatory is defined by the location vectors, termed here as the *baseline vectors*, linking all the pairs of aperture locations in the horizontal plane. Each baseline vector is associated with the time averaged, intensity fluctuation cross-correlation (i.e. the coherence magnitude data) collected by the aperture pairs. In the recent theoretical developments [6-10], each baseline vector was assumed unique, so that there were only a single coherence magnitude measurement per baseline vector. In this application it is time to exploit a previously existing and fairly obvious technique to further reduce integration time. The uniform tessellation of the aperture positions can be very useful because it allows redundant baseline vectors and their repeated and statistically independent coherence magnitude data to reduce noise.

To estimate the further reduction of integration time, it is assumed that the aperture positions occupy a square grid. This implies a square grid for both the u-v plane and the positioning of the pixels in the desired image field-of-view. In the latter case, the size of the image is denoted by N pixels on a side, where N is an odd integer. The following discussion demonstrates how a square grid of aperture positions that are $N+1$ on a side can produce a significant reduction of integration time by means of redundant baseline vectors.

To begin, we use Figure 6 to explain the process, where $N=11$. The figure shows $(N+1)^2 = 12^2$ apertures in a square array. We take ¼ of this array, shown by the red outlines, and compute the intensity fluctuation cross-correlations for all the baseline vectors in the $(N+1)/2$ by $(N+1)/2$ region. Then we reposition this array within the $(N+1)$ by $(N+1)$ array without repeating any position and without repeating a cross-correlation for a 180-degree rotation of a baseline vector. As is described below in Appendix A, which explains the computational aspects of the design, all of these calculations are readily parallelizable and therefore can be produced within the same integration time. Given this cross-correlation data, we can construct an $(N+1)/2$ by $(N+1)/2$ array, where for each of the fundamental baselines there is assigned the sample averages of the redundant coherence magnitude measurements.

Figure 6: The geometry of the aperture locations in the horizontal plane. $R(\mathbf{x}/\lambda)$ is the redundancy of the u-v plane baseline vector

The fundamental baseline vectors are shown at the top of Figure 7. Lower in the Figure the left-directed and right-directed vectors are sorted out preparatory to the construction of the u-v plane array. Notice that the left-directed vectors have no vectors on the lowest horizontal layer, and the right-directed vectors on the left-most vertical layer. The reason for this is that the intensity fluctuation cross-correlation is the same as that associated with its 180 degree rotation. This means that the pair of grids at the bottom of Figure 7 must be overlapped, joining the right-most vertical column of the left-hand array to the left-most vertical column of the right-hand array.

Figure 7: The fundamental baseline vectors (top), sorted into left-directed and right-directed vectors (bottom). These will be amalgamated into a central vertical column.

Figure 8: Construction of the u-v plane

Figure 9: Redundancy matrix for the N = 11 example.

The next step is the construction of the u-v plane as illustrated by Figure 8. The baseline vectors in that plane take the form of the basic measurements in the object plane divided by λ, the mid-band wavelength of the photodetection devices. The right side of the previous diagram is amalgamated as described previously; the right-hand array is then rotated 180 degrees counterclockwise. Then the left-hand array in the previous diagram is rotated 180 degrees clockwise and amalgamated along the horizontal seams. The result is a u-v plane array that has its origin at the center of the array and forms an $N \times N$ Fourier-domain matrix (the same dimensions as the image-domain matrix). Each baseline vector and its 180 degree rotation has the same sample averages of the redundant coherence magnitude measurements.

The resulting redundancy matrix for our $N = 11$ example is shown in Figure 9. In general, for each u-v vector, $\mathbf{u}$,the redundancy, denoted by $R(\mathbf{u})$ is determined as follows:

$$U \in \mathbb{R}^{N+1} : U = [1,...,1] \quad M \triangleq \begin{bmatrix} 0 & 0 & 0 \\ 0 & U^T U & 0 \\ 0 & 0 & 0 \end{bmatrix}$$
$$R(\mathbf{u}) = \begin{bmatrix} 0 \\ I_N \\ 0 \end{bmatrix}^T \left\{ M \circ \left\{ F^H \left[\left| F[M] \right|^2 \right] \right\} \right\} \begin{bmatrix} 0 \\ I_N \\ 0 \end{bmatrix} \tag{7}$$

We note that:

$$\left(\tfrac{1}{2}(N+1)+1 \right)^2 \le R(\mathbf{u}) \le (N+1)^2 \tag{8}$$

Furthermore, the sample averages of the redundant coherence magnitude measurements. Have the form:

Intensity fluctuation cross correlation for u-v vector $\mathbf{u}$

$$= \frac{1}{R(\mathbf{u})} \sum_{s=1}^{R(\mathbf{u})} \kappa^2 \eta^2 \frac{\Delta \nu_c}{\Delta \nu_d} \bar{\beta}^2 \left| \gamma(\mathbf{u}) \right|^2 P(A) + \frac{1}{R(\mathbf{u})} \sum_{s=1}^{R(\mathbf{u})} \left[\kappa^2 \eta \frac{\Delta \nu_c}{\Delta \nu_d} \bar{\beta} \right] \frac{1}{\sqrt{\Delta T \Delta \nu_d}} N_{\mathbf{u},s}(0,1) \tag{9}$$

where the $N_{\mathbf{u},s}(0,1)$ for all s and $\mathbf{u}$ are statistically independent. Since we assume that all apertures and their characteristics are the same as well as the integration time, we can divide all terms by $\left[\bar{\beta}\kappa^2\eta\,\Delta\nu_c/\Delta\nu_d\right]\Big/\sqrt{\Delta T\Delta\nu_d}$ to obtain the expression for the sample averages of the redundant coherence magnitude measurements of the empirical SNR to obtain:

$$S(\mathbf{u}) == S_0\sqrt{\Delta T(\mathbf{u})}\left|\gamma(\mathbf{u})\right|^2 + \frac{1}{R(\mathbf{u})}\sum_{s=1}^{R(\mathbf{u})} N_{\mathbf{u},s}(0,1) \qquad \text{(10. a-b)}$$
$$S_0 = \eta\bar{\beta}\sqrt{\Delta\nu_d}\,P(A)$$

The quantity $\frac{1}{R(\mathbf{u})}\sum_{s=1}^{R(\mathbf{u})} N_{\mathbf{u},s}(0,1)$ is of course a zero mean, Gaussian random variable with standard deviation:

$$\sigma\left(\frac{1}{R(\mathbf{u})}\sum_{s=1}^{R(\mathbf{u})} N_{\mathbf{u},s}(0,1)\right) = \sqrt{E\left\{\frac{1}{R^2(\mathbf{u})}\sum_{s=1}^{R(\mathbf{u})}\sum_{s'=1}^{R(\mathbf{u})} N_{\mathbf{u},s}(0,1)\,N_{\mathbf{u},s'}(0,1)\right\}} = \frac{1}{\sqrt{R(\mathbf{u})}} \qquad (11)$$

Hence, we obtain:

$$S(\mathbf{u}) == S_0\sqrt{\Delta T}\left|\gamma(\mathbf{u})\right|^2 + \frac{1}{\sqrt{R(\mathbf{u})}} N_{\mathbf{u}}(0,1) \qquad \text{(12. a, b)}$$
$$S_0 = \eta\bar{\beta}\sqrt{\Delta\nu_d}\,P(A)$$

However, the empirical SNR should be measured in comparison with a unit standard deviation. Then as before, we define:

$$SNR_d \,\square\, E\left[S(\mathbf{u})\sqrt{R(\mathbf{u})}\right] = S_0\sqrt{\Delta T\,R(\mathbf{u})}\left|\gamma(\mathbf{u})\right|^2 \;\Rightarrow\; \Delta T(\mathbf{u}) = \frac{1}{R(\mathbf{u})}\left[\frac{SNR_d}{S_0\left|\gamma(\mathbf{u})\right|^2}\right]^2 \qquad (13)$$

We now see that this version of ΔT is the same as $\{\Delta T\}_{conventional}$ except for the factor of $1/R(\mathbf{u})$. Then using the ratio $\{\Delta T\}_{NRPR}/\{\Delta T\}_{conventional}$ we obtain:

$$\Delta T = \frac{1}{R(\mathbf{u})}\left[\frac{4}{N_C S_0\left|\gamma(\mathbf{u})\right|^2_{\min}}\right]^2 \qquad (14)$$

For a quick upper bound estimate of the integration time, we can use $R(\mathbf{u}) \geq \left(\tfrac{1}{2}(N+1)+1\right)^2$. The upper bound for $R(\mathbf{u})$ is only four times larger than this lower bound. Furthermore the upper bound is quickly erased by the operation of NRPR because the upper bound is associated with the small baseline vectors which have the largest SNR, whereas the lower bound persists. Thus a truly precise estimate of ΔT, taking account of the operation of NRPR, is given by:

$$\Delta T = \frac{1}{\left(\tfrac{1}{2}(N+1)+1\right)^2}\left[\frac{4}{N_C S_0\left|\gamma(\mathbf{u})\right|^2_{\min}}\right]^2 \qquad (15)$$

Next, we consider the image field-of-view and stipulate some approximate requirements as illustrated in Figure 10. The x-y plane exists close to the geostationary object. Δx is the desired resolution length. We are looking at an illuminated (via reflected sunlight) object against a black sky. To achieve sufficient image detail, it is best to obtain a rough estimate of

Figure 10: Configuration of the image plane (the inverse Fourier transform of the u-v plane).

the object size. Also to provide sufficient black pixel constraints one should make the size of the whole image field-of-view approximately three times the size of the object. Given the resolution size, the size, *L*, of the entire array on the ground and the diameter of each aperture, *L*, and *d*, should be:

$$L \cong \frac{\lambda H}{\Delta x}, \quad d \cong \frac{L}{N+1} \tag{16}$$

where *H* is the geostationary altitude.

Next, we compute β , the number density per mode assuming diffuse reflection and using the black-body approximation and the apparent magnitudes of the satellites. Appendix B gives us:

$$\begin{gathered} S_0 = d^2 \eta Q\left(\nu_{peak}\right)\sqrt{\Delta \nu_d} \quad Q(\nu) = \frac{1}{kT\nu}\frac{F\left(m_{sat}\right)}{6\zeta(4)}\frac{\chi^3}{e^{\chi}-1} \\ \nu_{peak} = \left(1.0345\times 10^{11}\right)T_{\odot} \quad T_{\odot} = 5772\,K \quad \chi \equiv h\nu/kT \\ F\left(m_{sat}\right) = F_{\odot}\times 10^{0.4\left[-26.832-m_{sat}\right]} \quad F_{\odot} = 1350\,W/m^2 \end{gathered} \tag{17. a-g}$$

where $Q\left(\nu_{peak}\right)$ is the photon arrival rate, ν_{peak} is the frequency of the solar spectrum maximum, $F\left(m_{sat}\right)$ is the flux from a satellite of apparent magnitude m_{sat} and $\zeta(4)$ is the Rieman zeta function evaluated at 4.

4. Analysis and benefits of multispectral photodetector operation

An additional way that results in decreased integration time is due to the stipulation (2) in the Introduction, that the bandwidth of the photodetectors must be much smaller than the optical bandwidth. This is known as the slow detector assumption. The technique is to equipe each detector with multiple non-overlapping frequency channels (so that all channels are statistically independent) denoted here by M_c. One then averages the detector output channels as depicted in Figure 11 . The theory established by Brown and Twiss is that if each channel is at least an order of magnitude larger than the detector bandwidth, the SNR for M_c channels is increased in proportion to $\sqrt{M_c}$, thereby, in effect, increasing the detector bandwidth by $\sqrt{M_c}$ and decreasing integration time by M_c. To put it another way, under the slow detector condition, the SNR depends on the spectral radiance, not the total flux. This has been established by theory [1, Remarks following Equation (3.62)] and [2, Equation (2.13)] and experiment [3,4]. The expression for the integration time is amended to:

$$\Delta T \cong \frac{1}{M_c\left(\frac{1}{2}(N+1)+1\right)^2}\left[\frac{4}{N_C S_0 \left|\gamma(\mathbf{u})\right|^2_{\min}}\right]^2 \tag{18}$$

The state of the art in multi-spectral detectors admits of reasonably priced and modest numbers of frequency channels. As illustrated in the figure below, if $\Delta\nu_d = 1\,GHz$ and each spectral channel is $10\,GHz$ one can sustain 600 channels.

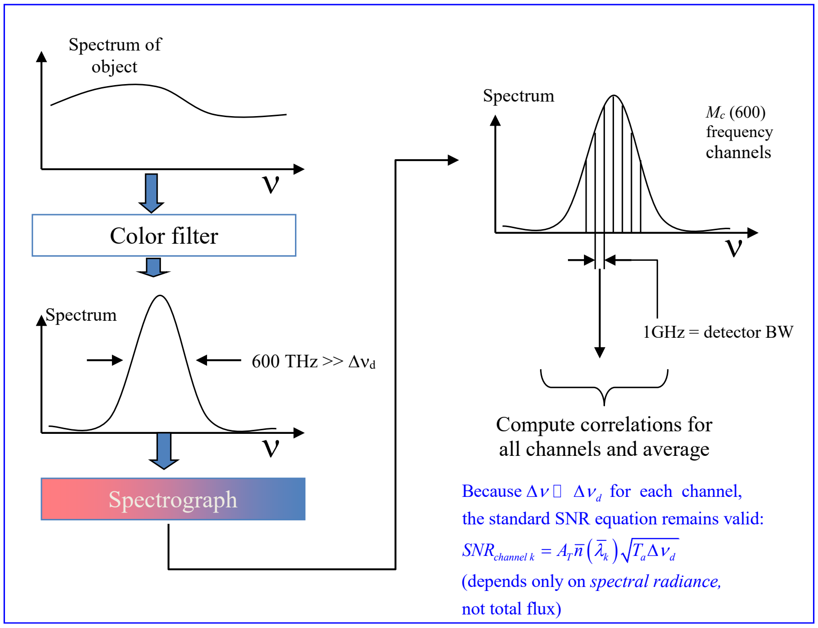

Because $\Delta\nu \gg \Delta\nu_d$ for each channel, the standard SNR equation remains valid:

$SNR_{channel\,k} = A_T\bar{n}\left(\bar{\lambda}_k\right)\sqrt{T_a\Delta\nu_d}$

(depends only on *spectral radiance,* not total flux)

Figure 11: illustrates the initial considerations in defining a multispectral correlator design. First one establishes the desired image resolution of the observed object. This drives the spectral resolution requirement which is implemented by a narrow band filter. inserted into the telescope optics and determines the optical bandwidth, $\Delta\nu$. We assume that $\bar{\beta}$ and the coherence are approximately constant over the optical bandwidth so that they are characteristic of the light in the entire band.

With further analysis, going beyond [1-4], the ratio of the frequency channels to the detector bandwidth need not be much larger than unity [16]. Thus $M_c \cong 6\times10^5$ can be attainable but requires further development and price reduction. In the next section, we will compare both 600 channels and 6×10^5.

5. Preliminary design of a high resolution ICI observatory

The first consideration is the range of the apparent magnitudes. Many of the smaller scale satellites range from magnitude 10 to 14. These are also typical of GOES 16 sized bodies. Therefore we select a satellite that is 6 by 6 meters, exhibiting m_{sat} in the range 10 to 14. We wish to achieve a fairly challenging degree of image resolution. Accordingly we choose $\Delta x = 10\,cm$. Taking account of the image field-of-view stipulations in Fig 10, namely $N \cong \left(3/\Delta x(m)\right)\times 6\,m \cong 2000$. This leads to:

$$L = 179m \quad d = L/\left(N+1\right) = 9\,cm \tag{19. a, b}$$

Additional parameters needed for the integration time computation are as follows:

$$H = 35{,}786\,km,\ \eta = 0.5,\ \Delta\nu_d = 1GHz,\ |\gamma|_{\min} = 10^{-3},\ N_C = \tfrac{8}{9}N^2 \tag{20. a-e}$$

A curious feature is the small aperture diameter and its effect on the partial coherence factor, $P(A)$. The following figure shows this factor as a function of the aperture width divided by the array width that would be able to resolve the illuminated object. Taking account of the fact that the object size is approximately one third of the array size, i.e. $d/\left(\frac{1}{3}L\right) = 0.13$, it is obvious that $P(A)$ is very close to unity. Now proceeding with $P(A)=1$ we compute the integration times and excess processing times using the formulae developed in the previous sections, namely Equations (14,15,16,17 and 18) and in the appendices A and B.

Table 1 displays the results for ΔT and ΔT_{excess} (as defined in Appendix A) In part (a), $M_c = 600$. Since $\Delta T_{excess} = 4.012\times10^{-5}$ the excess processing time has negligible effect on the total imaging time. At, $m_{sat} \cong 11.5$, ΔT is nearly an hour, but at $m_{sat} \cong 14$, $\Delta T \cong 85\,Hrs$ is still not prohibitive. In part (b), $M_c = 6\times10^5$. In this case $\Delta T_{excess} = 0.0401$ outweighs the lowest ΔT but becomes negligible above $m_{sat} \cong 12.5$. For all of the apparent magnitudes considered, $\Delta T + \Delta T_{excess}$ is never more than $\cong 5$ minutes. These results show an enormous reduction of imaging time as compared to the conventional Brown-Twiss SNR formulation. Indeed, the ratio $\left\{\Delta T\right\}_{NRPR}/\left\{\Delta T\right\}_{conventional}$ in the case $M_c = 6\times10^5$ is approximately 4.2×10^{-31}.

There is also a striking difference between the aperture design of Brown and Twiss and the present design. Figure 13 shows the Narrabri observatory with its more than six meter apertures, and the long baseline distances between them, whereas Figure 14 (which is termed the "compact array") envisions closely packed 9cm apertures. The earlier design was properly motivated by the goal of measuring stellar diameters, while the present design is absolutely driven by very high resolution imaging of resident space objects. The apertures in Figure 14

Figure 12: Calculation of the partial coherence factor in Ref [2] by means of the Manchester University Electronic Computing Machine. Square apertures are assumed. For the present observatory design the ratio of aperture size to the satellite size is very small, resulting in a near unit coherence factor.

$(a)\ M_C = 600, \Delta T_{excess} = 4.012\times10^{-5}$

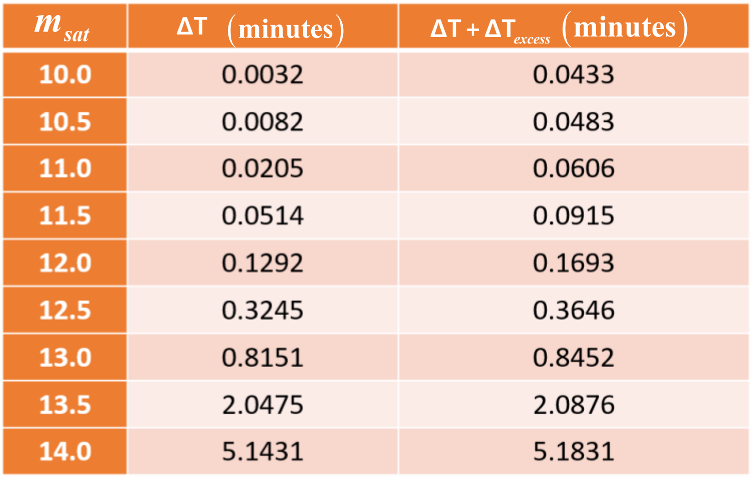

m_{sat}	ΔT (minutes)	$\Delta T + \Delta T_{excess}$ (minutes)
10.0	0.0032	0.0433
10.5	0.0082	0.0483
11.0	0.0205	0.0606
11.5	0.0514	0.0915
12.0	0.1292	0.1693
12.5	0.3245	0.3646
13.0	0.8151	0.8452
13.5	2.0475	2.0876
14.0	5.1431	5.1831

$(b)\ M_c = 6\times10^5, \Delta T_{excess} = 0.0401$

Table 1: (a) $M_c = 600$. Since $\Delta T_{excess} = 4.012\times10^{-5}$ the excess processing time has negligible effect on the total imaging time. (b) $M_c = 6\times10^5$. In this case $\Delta T_{excess} = 0.0401$ outweighs the lowest ΔT but becomes negligible above $m_{sat} \cong 12.5$.

Figure 13: Illustration of the Narrabri Observatory flux collectors; their size and spacing.

(b)

Figure 14: The compact array, showing closely spaced, highly redundant and very small flux collectors.

could be entirely enclosed units each consisting of a refractive lens with a Cholesteric Liquid Crystal (CLC) tunable aperture mirror controlling line of sight, feeding into a compound elliptical concentrator which deposits photons on a multispectral avalanche photodiode. Each aperture sends its intensity fluctuation signals into a processing mat which computes all the redundant coherence magnitude data.

The compact array design described above is one of a number of imaging devices that resemble imagers that occur in nature, namely the insect eye as shown in Figure 15. The insect eye has a wide field of view, but because it, like ICI, measures only intensity fluctuations, the partial coherence effect forces it to consist of a sheaf of tiny intensity sensors, called *ommatidia*. The individual ommatidia are not diffraction limited image forming devices. Each ommatidium has a lens that focuses light on a light guide (i.e. a transparent tube or *rhabdom*) which diffuses the light into closely packed photoreceptor cells (the *R-cells*).

Figure 15: Diagrams of the common insect eye. The flux collectors (ommatidia) must be too small to resolve the target, else the eye cannot work.

The rhabdom/R-cells geometry permits multispectral operation. The insect eye is a highly emergent, sophisticated intensity sensing device capable of very high resolution. Our suggested design for an ICI observatory in Figure 14 will be one of a number of design refinements based upon the study of insect eyes and the development of *artificial ommatidia*.

The study of nature for the advance of astronomy will also result in a vast reduction in the cost of high resolution imaging of geostationary satellites based on the ground. If we consider a ~180 meter primary mirror (to attain 10 cm resolution), seeing conditions would demand that the primary would be segmented (each segment being ~ 1 meter or less) and all segments controlled by active optics to reduce phase scintillations below roughly $\lambda/30$ in the visible range. The extreme restrictions on sensitivity also pertain to large-scale conventional interferometers. No conventional visible range multipixel imager has been developed or proposed with 4 Mega pixel imaging, and 10 cm resolution per pixel out to 36,000 km, with a cost below $ 140 million USD. In contrast, the specifications for optical alignments and surface precision for the present ICI concept are in the centimeters range not the nanometer range. In addition, the ICI aperture is fully enclosed, and temperature controlled. These features mean that the ICI apertures can be mass produced. Furthermore, although we mentioned a super-computer as a vehicle for parallelizing the redundant coherence magnitude computations, only addition operations are needed. Thus a reasonably simple *adding machine* will suffice to perform imaging within minutes or hours of integration time.

6. Concluding remarks and further efforts

This paper considered the design of an ICI observatory capable of imaging commercial geostationary satellites with a resolution of 10 centimeters and a field-of-view of four mega-pixels. The effects of redundant baseline measurements and multispectral photodetectors were included. The integration times were computed for apparent magnitudes spanning the range 10 to 14. For modest numbers of multispectral frequency channels, integration times spanned minutes to hours, and for more advanced multispectral sensors, the integration times were no longer than five minutes. The partial coherence effect tightly constrained the observatory design to be one in which small, independent apertures are closely spaced in a large square array (~180 meters on a side). This architecture strongly resembles that of the insect eye, which leads to both enormous imaging capability as well as inexpensive hardware. Further efforts will harness our study of nature to advance computational imaging via ICI considerably beyond conventional astronomical technology.

Appendix A

Here we consider the details of the algorithms needed to calculate the necessary intensity fluctuation cross-correlations and their insertion into the fundamental baselines needed to populate the u-v plane. Up to one thousand image pixels on a side (i.e. a megapixel image) are deemed sufficient to provide sufficient image resolution for many geostationary satellites. We begin with a number of definitions:

$C_{(\{k,j\}\rightarrow\{l,m\})}\left(m\delta t\right)$ □ The product of intensity flutuations for the baseline vector $\left(\{k,j\}\rightarrow\{l,m\}\right)$ within the aperture frame of rereference

$\{k,j\}$: $k =$ horizontal index of the aperture position relative to the below-left corner of the aperture array, marking the base of the baseline vector

$j =$ vertical index " " marking the base of the vaseline vector ...

$\{l,m\}$: are similarly defined and mark the tip of the baseline vector. These coordinate indices are shown in Figure 6.

$\delta t = 1/f$, f □ Sample frequency employed to calculate the time averaged intensity cross-correlations $\cong \Delta\nu_d$

i.e. the coherence magnitude data averaged over ΔT

$$\hat{C}\left(\{k,j\}\rightarrow\{l,m\}\right) = \sum_{m=1}^{\Delta T/\delta t} C_{(\{k,j\}\rightarrow\{l,m\})}\left(m\delta t\right) \quad \text{□ coherence magnitude data averaged over } \Delta T \text{ for baseline vector coordinates } \{k,j\}\rightarrow\{l,m\}\left(k,j\right) \text{ as defined in Figure A-1} \qquad \text{(A1. a-e)}$$

The quantities $\hat{C}\left(\{k,j\}\rightarrow\{l,m\}\right)$ are running averages that stop at the calculated integration time, ΔT . The intermediate values, $C_{(\{k,j\}\rightarrow\{l,m\})}\left(m\delta t\right)$, are not saved. These coherence magnitude data are to be calculated by means of separate analogue or digital computers that are resident in each ICI aperture. Because of the limit on $N \leq 2\times10^3$ each aperture processor needs to compute less than two thousand coherence magnitude values. This suffices to compute all the necessary $\hat{C}\left(\{k,j\}\rightarrow\{l,m\}\right)$ values simultaneously within the predicted integration time ΔT so that there is no excess computation time beyond ΔT .

Furthermore, the operation of NRPR quickly reduces the noise components of the small baseline vectors. Because of this, not all resident aperture computers need participate in computing the $\hat{C}\left(\{k,j\}\rightarrow\{l,m\}\right)$. In fact, only the smallest number, $\left(\frac{1}{2}\left(N+1\right)+1\right)^2$, of $\hat{C}\left(\{k,j\}\rightarrow\{l,m\}\right)$ must be computed. Let us define:

$$\begin{aligned}\mathrm{K}\left(\Delta x,\Delta y\right) = \text{The sum of all } \hat{C}\left(\{k,j\}\rightarrow\{l,m\}\right) \text{ that pertain to} \\ \text{the baseline vector, } \left(\Delta x,\Delta y\right) \text{ in the image plane}\end{aligned} \tag{A2}$$

Our analysis starts with the computation of the $\mathrm{K}\left(\Delta x,\Delta y\right)$ pertaining to the rightward pointing baselines in Figure 7. We note that because only coherence magnitudes are computed, not coherence phases, the baseline vectors are distinguished only by their lengths, and therefore the leftward pointing baselines are endowed with the same $\mathrm{K}\left(\Delta x,\Delta y\right)$ values. Likewise the same is the case for the lower pointing baselines shown in Figure 8. Hence, we need consider only the rightward pointing baselines in Figure 7.

Figure A-2, illustrates how the $\mathrm{K}\left(\Delta x,\Delta y\right)$ are composed of the $\hat{C}\left(\{k,j\}\rightarrow\{l,m\}\right)$ by summing the redundant coherence magnitude data pertaining to the (4,6) baseline In the in the image domain coordinates while using only $\left(\tfrac{1}{2}\left(N+1\right)+1\right)^2\left(=49\right)$ of them. The resulting $\mathrm{K}\left(\Delta x,\Delta y\right)$ is:

$$\begin{aligned}\mathrm{K}\left(\Delta x=4,\Delta y=6\right) = {} & \hat{C}\left(\{0,0\}\rightarrow\{4,5\}\right)+\hat{C}\left(\{1,0\}\rightarrow\{5,5\}\right)+\ldots+\hat{C}\left(\{8,0\}\rightarrow\{11,5\}\right) \\ & +\hat{C}\left(\{1,0\}\rightarrow\{5,5\}\right)+\hat{C}\left(\{2,0\}\rightarrow\{6,5\}\right)+\ldots+\hat{C}\left(\{8,0\}\rightarrow\{11,5\}\right) \\ & \quad\vdots \\ & +\hat{C}\left(\{0,4\}\rightarrow\{3,9\}\right)+\hat{C}\left(\{1,4\}\rightarrow\{4,9\}\right)+\ldots+\hat{C}\left(\{8,4\}\rightarrow\{11,9\}\right) \\ & \quad\vdots \\ & +\hat{C}\left(\{0,5\}\rightarrow\{3,10\}\right)+\hat{C}\left(\{1,5\}\rightarrow\{4,10\}\right) \\ & +\hat{C}\left(\{2,5\}\rightarrow\{5,10\}\right)\ +\hat{C}\left(\{3,5\}\rightarrow\{6,10\}\right)\end{aligned} \tag{A3}$$

Note that all other baseline vectors in the u-v plane will have the same number of terms and that for all redundant vectors in the u-v plane, all the $\hat{C}\left(\{k,j\}\rightarrow\{l,m\}\right)$ terms will be different. Thus for each pixel in the u-v plane there will be $\left(\tfrac{1}{2}\left(N+1\right)+1\right)^2$ terms, each one containing distinct coherence magnitude values. For an N^2 image , $\left(\tfrac{1}{2}\left(N+1\right)+1\right)^2 N^2$ coherence magnitudes must be summed, requiring the same number of Flops (Floating Point Operations). However, with existing super computers capable of 10^{18} Flops per second the excess time needed for this processing is

$$\Delta T_{Excess} = \left(\tfrac{1}{2}\left(N+1\right)+1\right)^2 N^2 \big/ 10^{18} \tag{A4}$$

For multispectral detectors, with M_c frequency channels, T_{Excess} becomes:

$$\Delta T_{Excess} = \left(\tfrac{1}{2}\left(N+1\right)+1\right)^2 N^2 M_c \big/ 10^{18} \tag{A5}$$

Figure A-1:

These numbers constitute the excess processing time needed to secure all the redundant baseline data beyond the predicted integration time. Thus both the integration time and the excess processing time will be displayed in the body of this paper.

Appendix B

This section derives S_0 characterizing the satellites by their apparent magnitude due to their diffuse reflection of solar radiation and its black body approximation. We begin with the black body law, $\Sigma(\nu)$, as a function of frequency ν. This is proportional to:

$$\Sigma(\nu) = \frac{\chi^3}{\exp(\chi)-1}; \quad \chi \equiv \frac{h\nu}{kT} \tag{B1.a,b}$$

If the total flux, F, of the satellite is known, the spectral radiance is given by:

$$B_\nu(\nu) = M\Sigma(\nu), \quad M = \tfrac{h}{kT} F \Big/ \int_0^\infty d\chi \frac{\chi^3}{\exp(\chi)-1} \tag{B2.a,b}$$

We now evaluate the denominator:

$$\int_0^\infty d\chi \frac{\chi^3}{\exp(\chi)-1} = \int_0^\infty d\chi \frac{\chi^3}{1-e^{-\chi}} = \sum_{n=1}^{\infty} \int_0^\infty d\chi\, \chi^3 e^{-n\chi} = 6\sum_{n=1}^{\infty} \frac{1}{n^4} = 6\zeta(4) \tag{B3}$$

where $\zeta(4)$ is the Rieman zeta function evaluated at 4. The $Q(\nu)$, the photon arrival rate is:

$$Q(\nu) = \frac{1}{h\nu} B_\nu(\nu) = \frac{1}{kT\nu} \frac{F(m_{sat})}{6\zeta(4)} \frac{\chi^3}{e^\chi - 1} \tag{B4}$$

We evaluate $Q(\nu)$ at the peak frequency of the Solar spectrum maximum:

$$\nu_{peak} = \left(1.0345 \times 10^{11}\right) T_\odot \quad T_\odot = 5772\,K \tag{B5. a, b}$$

where it is well known that $F\left(m_{sat}\right)=F_{\odot}\times 10^{0.4\left[-26.832-m_{sat}\right]}$ and $F_{\odot}=1350\,W/m^2$. In summary:

$$S_0=Q\left(\nu\right)=\frac{d^2\eta}{kT\nu}\frac{F\left(m_{sat}\right)}{6\zeta\left(4\right)}\frac{\chi^3}{e^{\chi}-1}\sqrt{\Delta\nu_d}\,,\quad \chi\left(\nu_{peak}\right)\approx\frac{h\nu_{peak}}{kT} \qquad \text{(B6. a, b)}$$

7. Back Matter

Funding. Excalibur Almaz, Inc., Augusta Quantum Electrodynamics Inc.

Acknowledgments. D. Hyland thanks Excalibur Almaz for its support.

Disclosures. The author declares no conflicts of interest.

Data availability. Data underlying the results presented in this paper are not publicly available at this time but may be obtained from the authors upon reasonable request.

Supplemental document. Not applicable.

References

1. R. Hanbury Brown, and R.Q. Twiss, " Interferometry of the Intensity Fluctuations in Light. I. Basic Theory: The Correlation between Photons in Coherent Beams of Radiation" ,*Proceedings of the Royal Society of London. Series A, Mathematical and Physical Sciences,* Vol. 242, No. 1230 (Nov. 5, 1957), 300-324.
2. R. Hanbury Brown, and R.Q. Twiss, " Interferometry of the Intensity Fluctuations in Light II. An Experimental Test of the Theory for Partially Coherent Light", *Proceedings of the Royal Society of London. Series A, Mathematical and Physical Sciences,* Vol. 243, No. 1234 (Jan. 14, 1958), 291-319.
3. R. Hanbury Brown, and R.Q. Twiss, " Interferometry of the Intensity Fluctuations in Light III. Applications to Astronomy", *Proceedings of the Royal Society of London. Series A, Mathematical and Physical Sciences,* Vol. 248, No. 1253 (Nov. 11, 1958), 199-221.
4. R. Hanbury Brown, and R.Q. Twiss, " Interferometry of the Intensity Fluctuations in Light IV. A Test of an Intensity Interferometer on Sirius A", *Proceedings of the Royal Society of London. Series A, Mathematical and Physical Sciences,* Vol. 248, No. 1253 (Nov. 11, 1958), 222-237.
5. R. Fienup, "Phase retrieval algorithms: a comparison," *Appl. Opt.* 21, 2758-2769, 1982.
6. D. C. Hyland, "Noise reducing phase retrieval," *Appl. Optics*, vol. 54 (33), pp.9728-9735 (2015).
7. D. C. Hyland. "Analysis of Noise Reducing Phase Retrieval", *Applied Optics,* vol. 55 (13), pp. 3493-3501 (2016).
8. D. C. Hyland, "Improved Integration Time Estimates for Intensity Correlation Imaging", *Applied Optics*, 61 (33), pp.10002-10011 (2022)
9. D. C. Hyland, "Algorithm for Determination of Image Domain Constraints for Intensity Correlation Imaging", *Applied Optics*. 61 (35), pp.10425-10432 (2022)
10. D. C. Hyland, "Analysis and Refinement of Intensity Correlation Imaging", *Applied Optics*, 62 (21), pp.5683-5695 (2023).
11. D. C. Hyland, "Intensity Correlation Imaging and the Massive Reduction of Integration Times". Invited presentation. *4th International Conference on Optics, Photonics and Lasers.* December 4-7. Sheraton Grand Hiroshima Hotel, Hiroshima, Japan.
12. G. B. Folland, and A. Sitaram, "The uncertainty principle: A mathematical survey". *The Journal of Fourier Analysis and Applications*, 3(3): 207-238, 1997.
13. DeBrunner, V.; Havlicek, Joseph P.; Przebinda, T.; Özaydin, M. (2005). "Entropy-Based Uncertainty Measures for $L^2\left(\mathbb{R}^n\right)$, $l^2\left(\mathbb{Z}\right)$, and $l^2\left(\mathbb{Z}/N\mathbb{Z}\right)$ With a Hirschman Optimal Transform for $l^2\left(\mathbb{Z}/N\mathbb{Z}\right)$ ". *IEEE Transactions on Signal Processing* ***53*** *(8): 2690.*
14. P. Billingsley, Probability and Measure, Third Edition, May 1st, 1995, Wiley Interscience, p.362.
15. Dembo A, Cover TM, and Thomas JA 1991: Information Theoretic Inequalities. IEEE Transactions on Information Theory 37(6):1501-1517, see Theorem 23 on page 1513.
16. D. C. Hyland, "Calculation of Signal-to-Noise Ratio for Image Formation Using Multispectral Intensity Correlation". SPIE International Symposium on Optics and Photonics, "Techniques and Instrumentation for Detection of Exoplanets III" Conference, Paper No. 6693-23, San Diego, CA, 26 -30 August 2007.
17. "Senses. Insect eyes". Insects and Spiders of the World. Volume 8: Scorpion fly - Stinkbug. New York: Marshall Cavendish. 2003. p. 459. ISBN 978-0761473428.
18. Edward Gaten (1998). "Optics and phylogeny: is there an insight? The evolution of superposition eyes in the Decapoda (Crustacea)". Contributions to Zoology. **67** (4): 223–236. doi:10.1163/18759866-06704001